Journal of Structural Biology 187 (2014) 103–111

Contents lists available at ScienceDirect

Journal of Structural Biology

journal homepage: www.elsevier.com/locate/yjsbi

Quantifying resolution limiting factors in subtomogram averaged cryo-electron tomography using simulations

Lenard M. Voortman [a], Miloš Vulović [a,b], Massimiliano Maletta [c], Andreas Voigt [d], Erik M. Franken [d], Angelita Simonetti [e], Peter J. Peters [b,c], Lucas J. van Vliet [a], Bernd Rieger [a,*]

[a] Quantitative Imaging Group, Department of Imaging Physics, Delft University of Technology, Lorentzweg 1, 2628 CJ Delft, The Netherlands
[b] Institute of Nanoscopy, Faculty of Health, Medicine and Life Sciences, Maastricht University, P.O. Box 616, 6200 MD Maastricht, The Netherlands
[c] NKI Netherlands Cancer Institute – Antoni van Leeuwenhoek Hospital, Plesmanlaan 121 B6, 1066 CX Amsterdam, The Netherlands
[d] FEI Company, Achtseweg Noord 5, 5651 GG Eindhoven, The Netherlands
[e] Architecture et Réactivité de l'ARN, Université de Strasbourg, CNRS, IBMC, 67084 Strasbourg Cedex, France

ARTICLE INFO

Article history:
Received 6 December 2013
Received in revised form 22 June 2014
Accepted 23 June 2014
Available online 3 July 2014

Keywords:
Cryo-EM
Tomography
Subtomogram averaging
TEM image simulation
Tilted CTF correction
Acquisition protocol
Ribosome

ABSTRACT

Cryo-electron tomography (CET) is the only available technique capable of characterizing the structure of biological macromolecules in conditions close to the native state. With the advent of subtomogram averaging, as a post-processing step to CET, resolutions in the (sub-) nanometer range have become within reach. In addition to advances in instrumentation and experiments, the reconstruction scheme has improved by inclusion of more accurate contrast transfer function (CTF) correction methods, better defocus estimation, and better alignments of the tilt-series and subtomograms. To quantify the importance of each contribution, we have split the full process from data collection to reconstruction into different steps. For the purpose of evaluation we have acquired tilt-series of ribosomes in such a way that we could precisely determine the defocus of each macromolecule. Then, we simulated tilt-series using the InSilicoTEM package and applied tomogram reconstruction and subtomogram averaging. Through large scale simulations under different conditions and parameter settings we find that tilt-series alignment is the resolution limiting factor for our experimental data. Using simulations, we find that when this alignment inaccuracy is alleviated, tilted CTF correction improves the final resolution, or equivalently, the same resolution can be achieved using less particles. Furthermore, we predict from which resolution onwards better CTF correction and defocus estimation methods are required. We obtain a final average using 3198 ribosomes with a resolution of 2.2 nm on the experimental data. Our simulations suggest that with the same number of particles a resolution of 1.2 nm could be achieved by improving the tilt-series alignment.

1. Introduction

Cryo-electron tomography (CET) is an essential technique to study the structure of macromolecules *in situ*, i.e. embedded in their native environment. A typical CET acquisition consists of a thin specimen that is tilted in order to acquire projections of the specimen at different angles. These projections are then used to reconstruct a three-dimensional (3D) volume. A major problem of this technique is radiation damage imposed by the electrons onto the specimen. This limits the amount of electrons that can be used for imaging which results in very noisy images. Nevertheless, this restriction can be overcome using subtomogram averaging. If a specimen contains many copies of an identical structure, the reconstructed subvolumes of these structures can be aligned and averaged to increase the signal-to-noise ratio (SNR) of the final reconstruction. Prerequisites for subtomogram averaging are that these copies can be identified in the reconstructed volume and aligned.

Projections in CET are intentionally recorded with underfocus. This defocusing allows contrast-generating interference of the undiffracted beam with the beam that is phase-shifted by the specimen. The contrast transfer function (CTF) describes the contrast transfer due to aberrations such as defocusing, astigmatism and spherical aberration. In effect, the CTF is an oscillating function of spatial frequency and depends on the defocus. These oscillations result in contrast inversions at certain spatial frequencies. Therefore, it is necessary to correct for the oscillations in order to interpret structures at a resolution beyond the first zero-crossing.

* Corresponding author. Fax: +31 15 2787640.
E-mail address: b.rieger@tudelft.nl (B. Rieger).

http://dx.doi.org/10.1016/j.jsb.2014.06.007
1047-8477/

Recently, different studies tackled a number of problems associated with CET. Due to the extremely low SNR per projection, defocus estimation requires either a special averaging technique (Fernández et al., 2006; Xiong et al., 2009), using magnification correction (Zanetti et al., 2009) or a new acquisition procedure (Eibauer et al., 2012). Due to the tilted geometry, required for tomography, CTF correction needs to account for the defocus gradient perpendicular to the tilt-axis (Philippsen et al., 2007; Voortman et al., 2011; Voortman et al., 2012; Winkler and Taylor, 2003; Fernández et al., 2006; Xiong et al., 2009; Zanetti et al., 2009). Furthermore, some researchers studied CTF correction methods that consider the defocus gradient within the specimen along the optical axis (Kazantsev et al., 2010; Jensen and Kornberg, 2000; Voortman et al., 2012). Using these methods together with subtomogram averaging, Eibauer et al. (2012) reported a resolution of 1.68 nm on mycobacterial membrane protein MspA.

Similar to single-particle analysis (SPA) (Rosenthal and Henderson, 2003), the resolution after subtomogram averaging depends on the number of particles but also on the accuracy of defocus estimation, CTF correction method as well as tilt-series and subtomogram alignment. In order to get a better understanding of what is currently limiting the resolution, it is needed to quantify the influence of the different processing steps.

In this study we investigate the influence of defocus estimation, CTF correction, tilt-series alignment and subtomogram alignment, primarily using simulations. We use an extended acquisition scheme to determine the defocus and defocus gradient for each projection in a tilt-series, providing us with orientation and planarity of the sample and thus the defocus at the positions of each macromolecule. We acquired experimental data using this scheme and simulate tilt-series which match the experimental conditions. After subtomogram averaging, we show that the experimental data is in good agreement with the simulations. Using these simulations we quantify the influence of defocus estimation and CTF correction, but also tilt-series alignment and subtomogram alignment on the resolution.

2. Experimental methods

2.1. Protein purification and sample incubation

Escherichia coli MRE600 were cultured up to an OD600 of 1.0. Then the cell membranes were disrupted in a French Press and the ribosomes were purified following the protocol described in Fechter et al. (2009).

The EF-G gene was inserted in *E. coli* following the procedure introduced by Dümmler et al. (2005). BL21 *E. coli* cells, transformed with the EF-G fuse gene, were cultured in LB medium at 37 °C up to an OD600 of 0.7. The expression of the EF-G was induced upon administration of isopropyl-β-D-1-thiogalactopyranoside (IPTG). Four hours after induction the cells were harvested and the pellet dissolved in a buffer containing 25 mM Tris–HCl pH 7.1, 5% glycerol, 700 mM NaCl, 6 mM β-mercapto-ethanol, 0.1 mM PMSF and 0.1 mM benzamidine. The cells were then lysed by sonication and the debris and cell-membranes were removed by centrifugation (13,000 rpm, 45 min). The EF-G was separated by the contaminants present in the lysate loading the cell extract in a nickel–nitrilotriacetic acid (Ni–NTA) chromatographic column. The column was washed with 5 volumes of buffer containing 25 mM Tris–HCl pH 7.1, 300 mM NaCl, 5% glycerol, 20 mM Imidazole, 6 mM β-mercapto-ethanol, 0.1 mM PMSF and 0.1 mM benzamidine and then the EF-G was eluted with a buffer containing 25 mM Tris–HCl, pH 7.1, 300 mM NaCl, 5% glycerol, 300 mM imidazole, 6 mM β-mercapto-ethanol, 0.1 mM PMSF and 0.1 mM benzamidine.

The purified 50S, 30S and EF-G were dialysed in separate membrane against the same buffer: 2 mM $MgCl_2$, 50 mM KCl, 20 mM Tris–HCl of pH 7.5, 0.1 mM EDTA, 1 mM DTT.

Equimolar amounts of 50S and 30S *E. coli* Ribosome were incubated for one hour with t-RNA fMet and m-RNA in a dialysis buffer. In another vial, with the same buffer composition, we incubated a 1.3 times excess of EF-G with a 10 times excess of fusidic acid. Then we mixed the solutions of the vials together in a 10 mM $MgCl_2$ buffer in order to obtain the 70S complex bound to t-RNA fMet and m-RNA and locked to EF-G by fusidic acid administration. 5 μL of 0.3 mg/mL of the complex were applied to glow-discharged quantifoil grids. The excess of liquid was blotted away in a vitrobot (FEI Company, 4 s blot time, Force 0, 100% humidity, 25 °C) and then the grid was flash-frozen in liquid ethane cooled down by liquid nitrogen.

2.2. Extended acquisition scheme

Improving the resolution beyond the first zero-crossing of the CTF requires a CTF correction step. In order to perform the CTF correction in such a way that it actually increases the resolution,

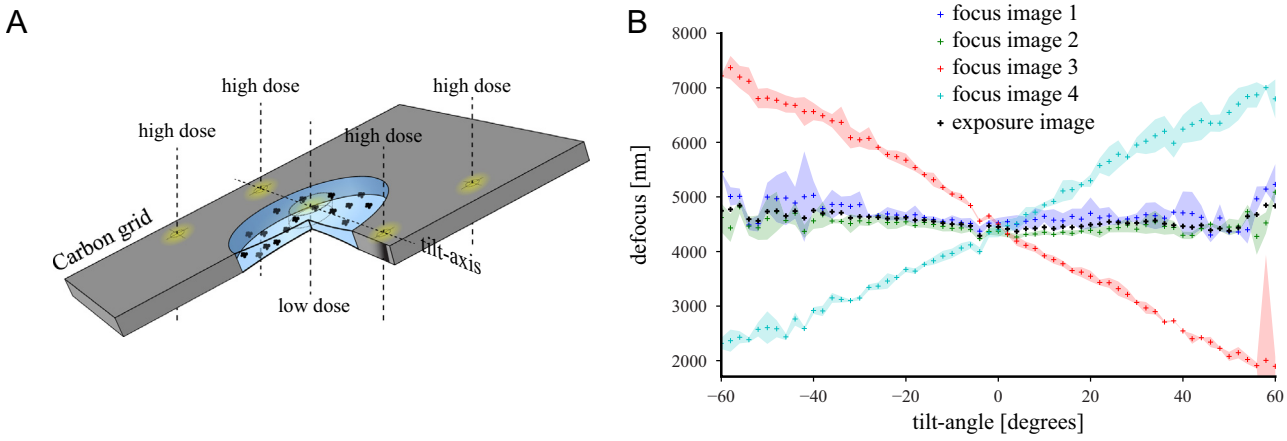

Fig.1. (A) Schematic overview of the extended acquisition scheme. The low-dose *exposure image* is located in a hole of the carbon-grid. Two high-dose *focus images* are located on the carbon, on the tilt-axis. The other two high-dose areas are located off-axis and positioned such that even at high tilt-angles the electron beam does not overlap with the *exposure image*. (B) Example of defocus estimation using the extended acquisition scheme. Four *focus images* are used to compute the defocus at the position of the *exposure image*. The color-shaded areas correspond to the uncertainty of the defocus estimate. (For interpretation of the references to colour in this figure legend, the reader is referred to the web version of this article.)

the defocus (gradient) of each projection must be estimated with a certain accuracy (Voortman et al., 2011). During the acquisition of a tilt-series, the defocus on the tilt-axis can vary due to the non-perfect mechanical properties of the stage, the accuracy with which the eucentric height can be adjusted, the auto-focus area being offset from the exposure area or other fluctuations.

Estimating the defocus on the low-dose exposures of a tilt-series is very challenging and usually requires averaging over a certain tilt-range (Fernández et al., 2006; Xiong et al., 2009). When acquired images at different angles need to be averaged, however, it is no longer possible to assess defocus variations throughout the tilt-series. Eibauer et al. (2012) introduced an extended acquisition scheme which can estimate the defocus per tilt-angle. They use two extra high-dose *focus images* per tilt-angle to estimate the defocus on the *exposure images*. We implemented and used an addition to this extended acquisition scheme. In addition to the two high-dose *focus images* which are positioned on the tilt-axis, we acquire two off-axis high-dose *focus images* (see Fig. 1A). Having now four high-dose images has a number of additional benefits. Firstly, we can estimate the orientation of the specimen which can be used for TCTF correction. Secondly, the accuracy might be improved since we have more measurements to base the defocus estimate on. Finally, having four areas allows us to check whether the specimen is flat.

The acquisition procedure was implemented in a development version of FEI's Tomography acquisition package (version 4.0), making use of the batch mode and automatic tracking and focusing. The low dose acquisition template (which allows for graphical selection of areas for focusing and tracking) was extended such that an arbitrary number of extra acquisition areas could be added. These may have their own optics and camera acquisition settings. We used these extra acquisition areas to acquire extra high-dose *focus images*.

Defocus estimation on these high-dose *focus images* and subsequent estimation of the specimen orientation and defocus of the *exposure images* is described in the Supplementary Material (S.M.).

Fig. 1B shows an example of defocus estimates on the four *focus images* and the resulting estimate of the defocus on the *exposure images*. The defocus estimation on the four *focus images* in this example was performed using the methods described previously in Vulović et al. (2012). The dose used for *focus images* was here only 4–5 times higher than for *exposure images* to minimize any potential radiation damage of the exposure area.

2.3. Data acquisition and reconstruction

Single axis tilt-series were collected at 300 kV, with a Titan microscope (FEI Company) equipped with a Falcon direct electron detector at NeCEN (www.necen.nl). The pixel size is 3.748 Å; the spherical and chromatic aberrations are both 2.7 mm, the objective aperture 100 μm, while the energy spread and illumination aperture are 0.7 eV and 0.03 mrad, respectively. We acquired projections from −60° to +60°, with an angular increment of 2°, a total dose around 78 $e^-/Å^2$ and a requested underfocus of 4.5 μm. CTF correction was performed using our previously developed publicly available toolbox (Voortman et al., 2012, http://www.diplib.org/add-ons). We used either regular CTF correction (CTF0) or tilted CTF correction (TCTF), details can be found in S.M. The tilt-series were reconstructed into tomograms using the standard IMOD procedure (Kremer et al., 1996; Mastronarde, 1997) after gold-bead tracking and rigid alignments. The mean absolute residual provided by IMOD from all gold markers was 1.83 pixels.

The tilt-series alignment included solving for all tilt-axis rotations, all magnifications and grouped tilt-angles. Distortions or local-alignments were not used. We selected the best four volumetric reconstructions for further analysis based on optimal defocus estimation and lowest residual in tilt-series alignment.

For particle picking we followed the standard PyTom procedure (Chen et al., 2013). We used a template of a ribosome (EMD-1920, Elmlund et al. (2013)) low-pass filtered to 4 nm resolution in order to localize similar structures in the tomogram using cross-correlation. The ribosomes were sorted for false positives based on their shape. After this cleaning procedure we obtained 3198 ribosome particles.

After particle picking, the location and orientation of each particle were refined using PEET (Nicastro et al., 2006). As an initial template we used a reference potential low-pass filtered to a resolution of 5 nm. The reference potential was generated from a high resolution X-ray structure as deposited within the RCSB Protein Data Bank (for details see Section 3.1). We iteratively refined the orientation estimate using six steps with 4× binning, followed by two steps with 2× binning and one final orientation refinement step on unbinned data.

We filter the averaged subvolume to correct for the damping of high spatial frequencies due to the modulation transfer function (MTF) of the camera and processing artifacts. This is done by weighting the angular-averaged power-spectra of the reconstructed volumes to match the angular-averaged power-spectra of the simulated interaction potential of the ribosome. This effectively amplifies the high spatial frequencies. After weighting of the power-spectra, the volumes were low-pass filtered to the resolution found by thresholding the Fourier shell correlation (FSC) calculated on two half datasets at 0.143.

3. Simulations

3.1. Tilt-series

An advantage of using a TEM image simulator is that it predicts the outcome of the data acquisition for many combinations of experimental parameters. We used the *InSilicoTEM* simulator (Vulović et al., 2013) to generate synthetic tilt-series with similar imaging conditions (defocus, dose, magnification) as in our experimental data in order to investigate the influence of defocus estimation, tilt-series alignment, sub-tomogram orientation estimation, and number of particles on the final resolution.

We simulated six tilt-series each containing 600 ribosome particles. As in the experiments, the tilt angles ranged from −60° to 60° in steps of 2° resulting in 61 (4k × 4k) unbinned images with a pixel size of 3.748 Å. Fig. 6 in S.M. shows an example of experimental and simulated projection, as well as slices from a tomogram.

The main steps in our image simulations are (i) construction of the specimen's interaction potential, (ii) modeling the electron–specimen interaction, (iii) propagation of the electron wave through the optics, and (iv) detection of the intensity.

The ribosome particles were embedded in a slab of vitreous ice modeled as a continuous medium with a potential of 4.5301 V. The thickness of the specimen was taken to be ∼35 nm and used to model the signal damping due to the plasmons of the vitreous ice. The voxel size was chosen to be the same as the pixel size in the images (3.748 Å) resulting in a specimen volume with a size of 4k × 4k × 81. The volume was divided in *x* and *y* directions into 25 × 25 subvolumes in which particles were randomly positioned. The input for computing the interaction potential of an individual particle was a high resolution X-ray structure as deposited within the RCSB Protein Data Bank (PDB). To simulate the whole ribosome particle, we combined the PDB entries 2WRJ (large ribosome subunit) and 2WRI (small ribosome subunit with elongation factor G). The coordinates of each combined PDB (2WRI + 2WRJ) were

Fig.2. Overview of the different post-processing steps that were applied to the simulated data. For the defocus estimation, CTF correction, tilt-series alignment and subtomogram alignment steps two different variations were used resulting in 16 different subtomogram averaged results.

rotated with random Roll–Pitch–Yaw angles (Kuffner, 2004) producing uniform sampling of particle orientations. Rotation was performed on PDB coordinates before calculating the final potential map to avoid interpolation errors. Finally, the interaction potential was calculated as the sum of the individual atomic potentials that were computed as the Fourier transforms of tabulated electron scattering factors. Prior to down-sampling to the pixel size, the resulting potential maps were low-pass filtered (Gaussian with standard deviation of 3.61 Å) in order to avoid aliasing. The influence of pH and the ions in the solvent is neglected as well as possible beam-induced motion.

The electron–specimen interaction was modeled via the thick-phase grating approach (TPGA) (Vulović et al., 2014) to account for the effects of the specimen thickness and tilt geometry. Our implementation of the TPGA utilizes non-uniform fast Fourier transform sampling of the parabolic Fresnel propagator in the frequency domain, to speed-up the calculations (Voortman et al., 2011, 2012).

The electron wave exiting the specimen is further subjected to the effective CTF which is simulated using the parameters of the Titan microscope described in Section 2.3. The applied defocus per projection for the simulations matched the values of the previously estimated defocus from the experimental datasets (estimated using the extended acquisition scheme) of on average 4.51 μm underfocus. Astigmatism was neglected.

The installed detector (Falcon I) was characterized using tools provided in Vulović et al. (2010). Conversion factor, MTF and detective quantum efficiency (DQE) of the detector were included in the model as described in Vulović et al. (2013). The integrated electron flux for each complete tilt-series was 78 $e^-/Å^2$.

Additionally, we wanted to compare the detector used in the experiments to a new generation of direct electron detectors in counting mode. Under ideal circumstances, such a detector in counting mode can be approximated as a *perfect* pixelated detector. Having square pixels of finite size, the detector's MTF is represented as a 2D sinc function (MTF = $\mathrm{sinc}(q\Delta x)$, where Δx is the pixel size) while the DQE of such detector is modeled as DQE = $\mathrm{sinc}^2(q\Delta x)$ (McMullan et al., 2009).

3.2. Post-processing

The simulated data was processed in the same way as the experimental data, see Section 2.3, except for a few differences due to the nature of the simulations.

In the simulated tilt-series the defocus varied per tilt-angle (matching the experimental data). For the defocus estimation two different options were used. A defocus estimation procedure that accounts for the varying defocus in a tilt-series (such as the extended acquisition protocol) was emulated by using varying defocus values. To simulate defocus estimation procedures which only estimate an average defocus for the entire tilt-series, the defocus values of an entire tilt-series were averaged and this average was then used to correct all projections in that tilt-series.

Tilt-series alignment is not required since the projections were simulated with perfect alignment. In order to estimate the alignment accuracy of the experimental tilt-series together with any eventual beam-induced motion, gold-bead tracking was performed on all gold markers within the field-of-view. Using all gold markers gives a good indication of the global misalignment but the alignment itself was performed using a manually selected subset. The mean residual from all gold markers was 1.83 pixels (as provided by IMOD) and was used to introduce a certain misalignment in the simulated tilt-series. The projections in the simulated tilt-series were randomly displaced using a Gaussian distribution with a standard deviation equal to the mean residual of all gold markers after alignment of the experimental tilt-series. Here we assume that random shifting of the projections produces a similar response as the true effects related to the misalignment of the real particles. This assumption is justifiable since each particle is simulated with different orientations and in that way a bias is avoided.

We did not simulate any debris or contamination in the tilt-series. As a result, all particles present in the reconstructed volumes are identical and easy to identify. Therefore, the simulated datasets are not representative to verify particle picking and subsequent classification procedures. Instead, we used the locations that were used in the simulations. To compare the simulations with the experiments, however, we must analyze the resolution for different numbers of particles to see whether particle picking was successful in the experimental data.

Subtomogram alignment was carried out equivalently to the experimental data processing. Since the simulated orientations were known, however, a *perfect* subtomogram alignment was also created.

Simulated data was processed with all different combinations of the aforementioned post-processing steps, leading to 16 different subtomogram averaged results (see Fig. 2).

4. Results

4.1. Experimental data

After processing the experimental data as described in Section 2.3, the final subtomogram average was calculated together with the corresponding FSC. The FSC was calculated by splitting the dataset in two after the subtomogram alignment. By thresholding the FSC at 0.143 we measured a resolution of 2.2 nm. In order to correctly interpret the electron microscopy map we fitted the PDB structure of a ribosome bound to EF-G (2WRJ, 2WRI) to the map. The rigid body fitting was performed using the `Fit in Map` function of Chimera (Pettersen et al., 2004) and is shown in Fig. 3A. It is clear that all the densities are occupied by the features of the 70S ribosome and we can observe that the EF-G (red in the picture) nicely fits in the protruding density left empty by the 70S. This confirms that the fucidic acid that we introduced in the solution stalled the ribosome in the late elongation state where the 70S is bound to EF-G.

The FSC in Fig. 3A for different number of particles, shows that the increase in correlation between 800 and 1600 is very small. Comparing the FSCs of Fig. 3A and B, we note that the FSCs match well for 100–800 particles. However, for the simulations (where all picked particles are identical) the correlation shows a larger

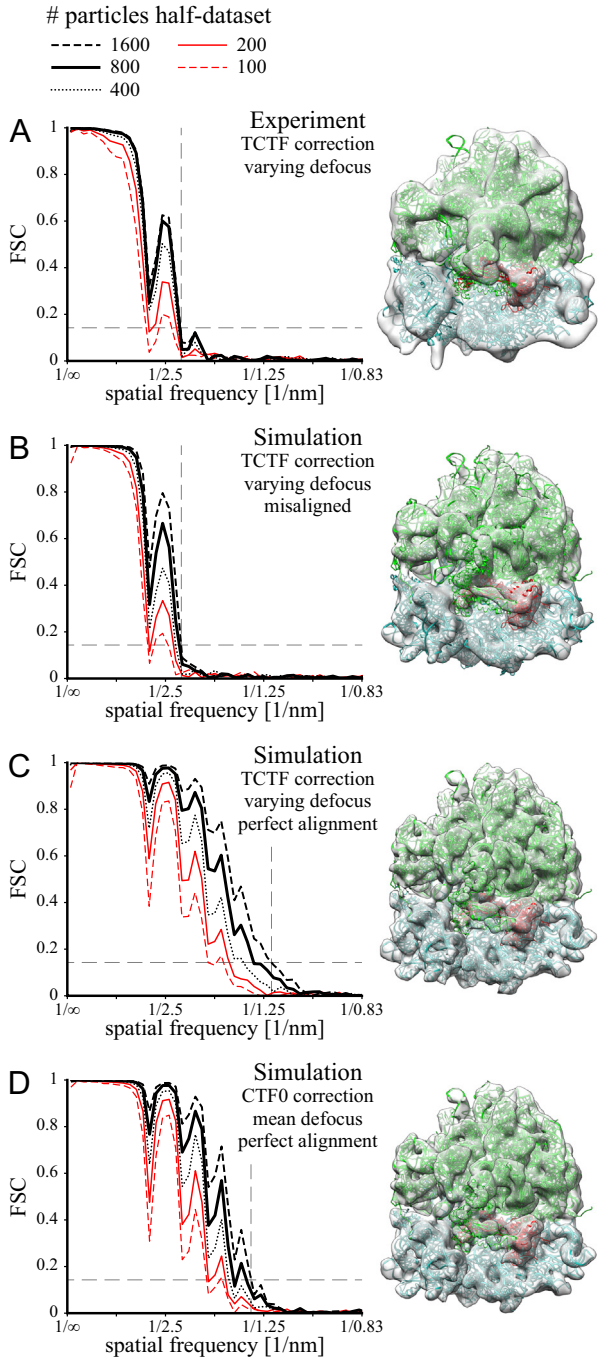

Fig.3. Fourier shell correlation (FSC) and isosurface representations for experimental and simulated data using different post-processing steps. (A) Experimental data, TCTF correction, varying defocus. (B) Simulated data, TCTF correction, varying defocus, misaligned. (C) Simulated data, TCTF correction, varying defocus, *perfect* alignment. (D) Simulated data, CTF0 correction, mean defocus, *perfect* alignment. Visualizations using Chimera (Pettersen et al., 2004), EF-G is highlighted in red.

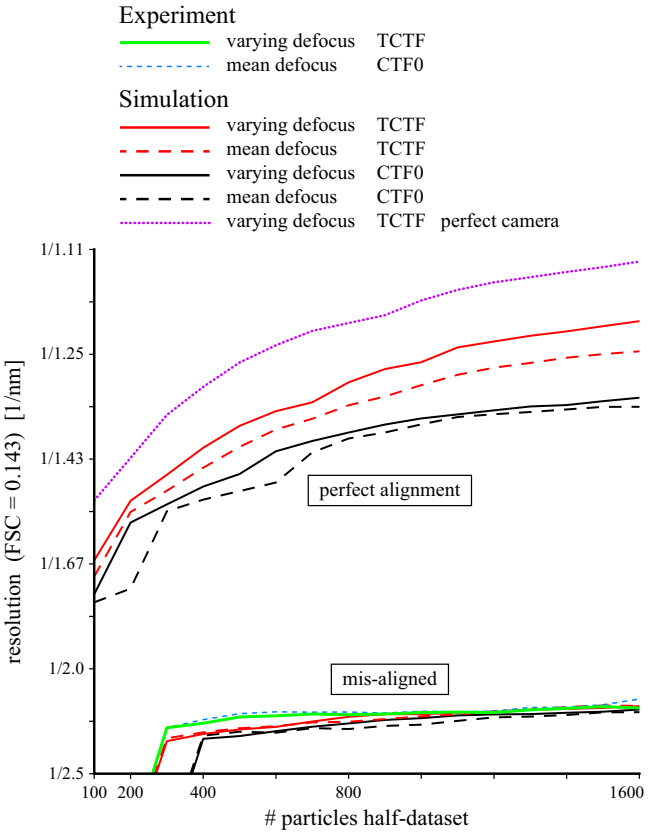

Fig.4. Resolution (FSC = 0.143) as a function of the number of particles, for experimental data and simulations. For the experiments and simulations with matching misalignment of the tilt-series, the resolution is slightly lower than 2 nm. The simulations with *perfect* tilt-series alignment show a clear influence of CTF correction and defocus estimation. The expected influence of a direct electron detector in counting mode (*perfect* camera) is also included (purple dotted line). (For interpretation of the references to colour in this figure legend, the reader is referred to the web version of this article.)

increase for 1600 particles. This might indicate that the total set of picked particles in the experimental data does not have a uniform quality.

The relation between the number of averaged particles and the final resolution is shown in Fig. 4. Using a threshold of 0.143 on the FSC we determine the resolution for different numbers of particles in each half-dataset. From Fig. 4 it is clear that the resolution only increases gradually. The sudden decrease in resolution for 100 and 200 particles is caused by the FSC dropping below 0.143 around the first zero-crossing.

There was only a minute difference between the resolution with TCTF or CTF0 correction. Similarly, the choice between a varying defocus estimate and the mean defocus estimate only has a small influence on the resolution.

All FSC curves presented in Fig. 3 show strong oscillations caused by the zero-crossings of the CTF. Given the amount of defocus variation in this dataset, we expect these oscillations to appear. The appearance of these oscillations, however, is also influenced by how the FSC is computed (see Section 3 in S.M.).

4.2. Simulated data

The processing chain of simulated tilt-series matched that of the experimental data as good as possible. Fig. 3B shows the FSC and isosurface renderings on simulated data. The resolution from the simulated data is in good agreement with the experimental data in Fig. 3A. Furthermore, the FSC shows similar characteristics. We also see that the molecular structure fits accurately inside the isosurface rendering. This demonstrates self-consistency of the procedures since the simulations used this molecular structure to generate projections.

The simulations indicate that the tilt-series alignment has the largest influence on the final resolution. Fig. 3C and D show the FSC and isosurface renderings for simulations where the tilt-series

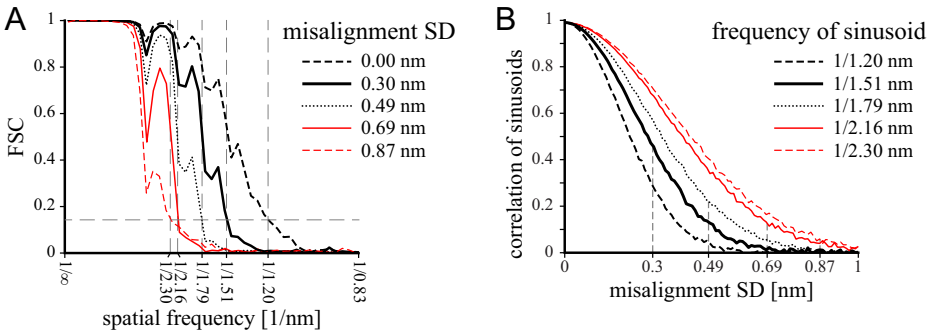

Fig.5. (A) Fourier shell correlation (FSC) of simulated data using 1600 particles in each half-dataset, TCTF correction and varying defocus for different amounts of misalignment. (B) Average normalized correlations of two sinusoids with frequencies chosen to correspond to the resolutions (FSC = 0.143) found in (A). One of the sinusoids was randomly displaced using a Gaussian distribution. The standard deviation (SD) of this random displacement is used as a measure for misalignment.

alignment was *perfect*. From the FSC it is clear that TCTF correction and varying defocus estimation results in an improvement of the FSC and thus also in an improvement of resolution.

In Fig. 4 the resolution is plotted as a function of the numbers of particles. The simulations were performed using different combinations of post-processing steps (see Fig. 2). The effects of the defocus estimation, CTF correction and tilt-series alignments are shown in Fig. 4. The influence of subtomogram alignment was relatively small and therefore omitted from the figure.

From Fig. 4 it is clear that with an inadequate tilt-series alignment, there is almost no influence of the type of CTF correction or defocus estimation on the attained resolution. However, with *perfect* tilt-series alignment, TCTF correction and varying defocus estimation are of clear influence. Also note that the influence of the varying defocus estimate has a larger influence when used in combination with TCTF correction.

The root-mean-square difference between mean defocus and varying defocus estimation as used in the simulations was 154 nm; this corresponds to a resolution of 1.15 nm using Eq. (7) in S.M. From these limits, we expect that using the mean instead of varying defocus estimation has a smaller influence on the attainable resolution than using CTF0 instead of TCTF correction. This is confirmed in Fig. 4. However, we see in the simulations that already for lower resolutions there is a notable improvement using TCTF correction and varying defocus estimation. It is expected that using a *perfect* camera (direct electron detector in counting mode) a certain resolution can be achieved with approximately half the number of particles (dotted purple line in Fig. 4).

The amount of misalignment that was introduced in the simulations was 1.83 pixels (~0.69 nm). From Fig. 4 we see that this limits the resolution to 2.2 nm. To better understand the influence of a certain misalignment on the FSC, we processed tilt-series using different amounts of misalignment. Fig. 5A shows the FSC of a reconstruction similar to those presented in Fig. 3B and C. Then, we investigated the influence of a certain misalignment on the obtained resolution. To this end, we calculated the correlation of two sinusoids of which one was randomly displaced. The frequency of the sinusoids was chosen to be the same as the obtained resolution in Fig. 5A. Fig. 5B shows that at a spatial frequency of $1/2.2\ \mathrm{nm}^{-1}$, a misalignment of ~0.69 nm results in a correlation of less than 20%.

To study the accuracy of the subtomogram orientation estimation, we compare the estimated (Euler) angles with the simulated angles. In order to quantify the difference between two sets of angles we first convert each set of angles to a rotation matrix with R_s the simulated rotation and R_e the estimated orientation. Now the orientation error can be found using $\mathrm{trace}(R_e R_s^{\top}) = 1 + 2\cos(\theta)$, where θ is the rotation angle required to rotate from R_s to R_e.

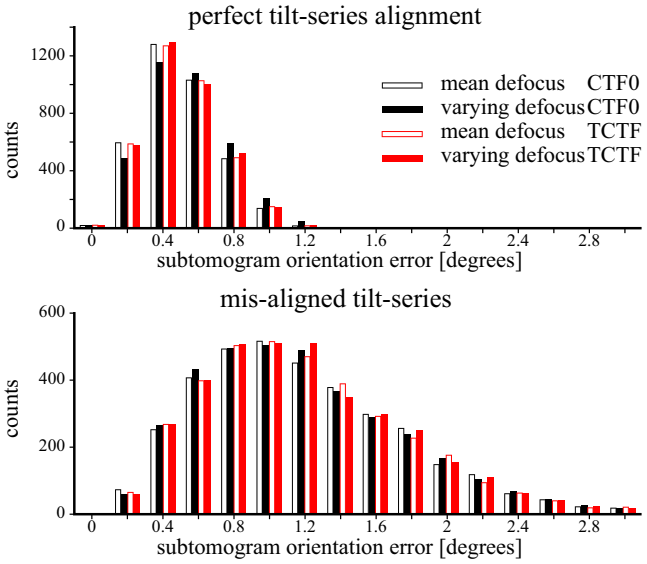

Fig.6. Accuracy of subtomogram alignment on simulated data using different post-processing procedures. Different CTF correction or defocus estimation methods do not seem to influence the orientation estimation. The tilt-series alignment does influence the subtomogram alignment. An angular mismatch of 2° corresponds to a 0.5 nm shift at the periphery of the ribosome.

Fig. 6 shows a histogram of the angular mismatch between the simulated orientations and the estimated orientations. It is clear that the orientation estimation is successful. The average orientation error for *perfect* tilt-series alignment or misaligned tilt-series result in a displacement of only ~0.1 nm and ~0.3 nm respectively at the periphery of the particle. This is also confirmed by the FSC of the simulations with *perfect* subtomogram alignment which is very similar to the FSC in which the orientation was estimated.

5. Discussion

The simulations are in good agreement with the experimental data which provides a good validation of the *InSilicoTEM* simulator (Vulović et al., 2013). These simulations allow us to conclude which processing steps need to be optimized in order to achieve a better resolution. Tilt-series alignment has the strongest influence on the final resolution, followed by the CTF correction method (CTF0 versus TCTF correction) and defocus estimation accuracy (varying defocus estimate versus mean defocus estimate).

The subtomogram alignment had the least significant influence on the resolution. In other words, the subtomogram alignment is already sufficiently accurate. It must be noted that the advantage of TCTF correction over CTF0 correction depends on the used field-of-view (here the field-of-view was 1.54 μm).

We used an FSC threshold of 0.143 to determine the resolution since it is expected from theory that this is a good indicator for the true resolution of the map in the absence of overfitting (Scheres and Chen, 2012; Rosenthal and Henderson, 2003). We are confident that the presented results do not suffer from overfitting since for the simulated data exchanging the estimated orientations with the simulated orientations did not influence the FSC and resolution. A different threshold criterion, e.g. 0.5 or half-bit criterion, would lead to slightly different resolutions. Nevertheless, this does not alter the relative difference between the different processing methods discussed in this study.

Here, we used an extended acquisition scheme and developed a tool for assessing the specimen geometry. Although in the case of a reasonably thin and flat specimen, four positions (instead of only two on the tilt axis) do not notably improve defocus estimation, they are still useful for checking specimen orientation and planarity. Furthermore, the extra off-axis regions do not have to be acquired for all tilt angles. A couple of images of (un)tilted focus areas will be sufficient to estimate the orientation and planarity of the specimen.

In Fig. 1A in S.M. we predict a resolution from which CTF0 correction would damp the FSC by more than 25%. Furthermore, in Fig. 1B in S.M. we predict the same threshold depending on the defocus estimation accuracy. For a comparison, we extended Fig. 4 with these resolution limits and included it as Fig. 2 in S.M. showing that the limits are in agreement with the results from simulations. A damping of 25% is relatively strong and we see in the simulations that already for lower resolutions there is a notable improvement using TCTF correction and varying defocus estimation. Similarly, Fig. 1 in S.M. depends on the chosen threshold value of 0.75. Changing the threshold will shift the boundaries between the regions but does not change the relative positions. From Fig. 2 in S.M., however, we conclude that the choice for 0.75 does provide a good indication of the resolution at which the influence of CTF correction or defocus estimation becomes relevant. Furthermore, the relative importance of defocus estimation and CTF correction was predicted correctly using criteria from S.M. independent of the chosen threshold.

Our estimate of the influence of defocus estimation accuracy is in good agreement with an estimate given by Schur et al. (2013). They estimated that a normally distributed defocus error with a uncertainty of ~100 nm results in a 50% attenuation at 0.8 nm (their Fig. 1B), using Eq. (7) in S.M. we predict a 43% attenuation. Zanetti et al., 2009 find that up to a resolution of about 1.8 nm one can tolerate a defocus estimation uncertainty of 500 nm. We predict, however, that in this scenario the signal is already attenuated by 42% which is in accordance with Schur et al. (2013). Here we explicitly take into account the resolution dependence of the transfer function, whereas in one of our earlier studies (Voortman et al., 2011) we only implicitly did so.

The resolution that we obtained here for the 70S ribosome (2.2 nm) is comparable with the one obtained by Chen et al. (2013) (2.1 nm) for a similar structure. Other studies reported resolutions of ~1.7 nm (Eibauer et al., 2012; Briggs et al., 2009) for particles with higher symmetry. For simulated particles with a *perfect* tilt-series alignment, however, a resolution up to 1.2 nm can be attained, see Fig. 4. This underlines the importance of tilt-series alignment which is apparently essential to improve the resolution. Here we used rigid alignments in IMOD. We did not use the possibility for local alignment since at this magnification there were not enough gold markers to produce a reliable local fit.

One approach to tackle the alignment problems involves a combination of SPA and subtomogram averaging techniques as in Zhang and Ren (2012); Bartesaghi et al. (2012). They used subtomogram averaging to assign initial locations and angles to each subvolume and then refine the alignment of the original projections using a projection matching procedure. In this way the final alignment is effectively independent of the initial tilt-series misalignment or rotation of the particles during tilt-series collection. Another benefit is that this method reduces the interpolation steps required to produce the intermediate steps in classic subtomogram averaging. Using this technique, Bartesaghi et al. (2012) reported a resolution of ~0.8 nm using 140,000 asymmetric units.

Recently, Schur et al. (2013) reported a resolution of 0.85 nm using an optimized data collection protocol. To achieve this resolution they averaged 242,692 asymmetric units. Instead of measuring the defocus changes throughout the acquisition of a tilt-series, they used an optimized protocol that effectively stabilized the stage movement and defocus.

When we extrapolate our simulation results to the same number of asymmetric units, the predicted resolution is in the same range. Fig. 7 provides a graphical comparison of the resolution with respect to the number of particles reported in Bartesaghi et al. (2012); Schur et al. (2013); Eibauer et al. (2012); Chen et al. (2013). Our extrapolation is based on methods presented in Rosenthal and Henderson (2003) and the data is exactly the same as in Fig. 4. Please note that the achieved resolution inevitably depends on the scattering properties of the studied structure. Therefore, one should be careful when interpreting the results from Fig. 7. Nevertheless, it is interesting that the resolution reported by Bartesaghi et al. (2012) is higher than the extrapolation of our optimal result. This is possibly due to a different reconstruction method, lower electron energy (80 kV), which provides higher contrast and a different detector.

We conclude that in our dataset suboptimal tilt-series alignment limits the resolution to around 2.2 nm. The origin of this misalignment is not easy to assess. By performing gold-bead

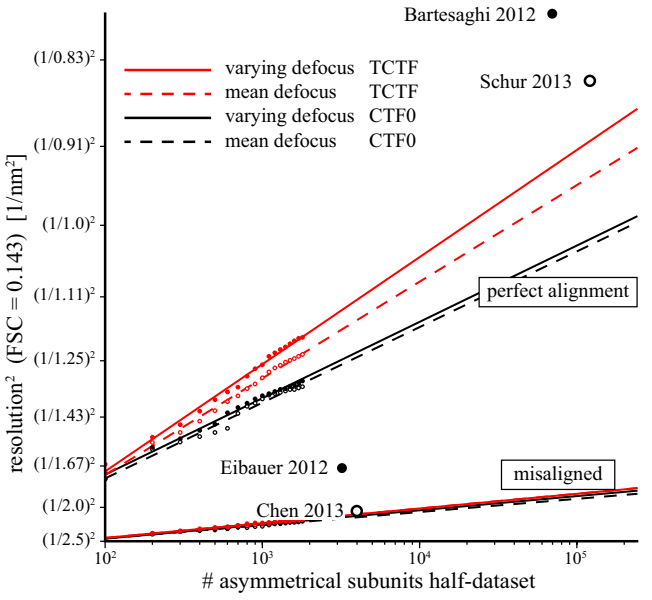

Fig.7. Extrapolation of resolution as a function of the number of particles. Different data points of related publications (Bartesaghi et al., 2012; Schur et al., 2013; Eibauer et al., 2012; Chen et al., 2013) of various structures are plotted for comparison. The horizontal axis represents the number of asymmetric units. The results from this study are extrapolated assuming a particular falloff of the particle's structure factor (see main text for details).

tracking on all gold markers within the field-of-view, we measured an alignment residual of approximately 1.83 pixels (~0.69 nm). As we see from Fig. 5, this misalignment results in a severe damping of correlation between sinusoids with a period of 2.2 nm. This indicates that the residual of the gold-bead tracking is a good indication of the amount of misalignment. Furthermore, we see that a seemingly small alignment residual of ~0.69 nm already has a large influence at a resolution of 2.2 nm.

In this study, we could not further investigate the influence of radiation damage. The damage to the structure of the ribosome is difficult to quantify. In fact, there is no model to accurately simulate the degradation of the structure. Recent studies (Bartesaghi et al., 2012; Schur et al., 2013) suggest, however, that using 25–40 $e^-/Å^2$ improves the resolution of the final average. Nevertheless, our simulations without influence of radiation damage accurately matched the experiments. If radiation damage is small and at random places, the majority of the particles will dictate the result at any location and *hide* the radiation damage.

Experimental data were acquired without an energy filter. In general, it is expected that energy filtering will improve the contrast. However, due to the thin ice the difference between energy filtered and unfiltered data might be inconspicuous. The reported simulation results do not include amplitude contrast. We did, however, simulate tilt-series with amplitude contrast but did not find a noticeable influence on the final resolution after subtomogram averaging.

The tomograms were acquired on very thin ice. This might make the ice more susceptible to beam-induced motion (Brilot et al., 2012). Therefore, the measured and simulated alignment error is a combined effect of the limited accuracy of the gold-bead tracking and the apparent beam-induced motion. Before a tomogram acquisition, the exposure area was visually inspected (in order to check the presence of ribosomes) with a dose of 1 $e^-/Å^2$. This pre-irradiation should have lowered the potential effects of beam-induced motion (Brilot et al., 2012).

The latest generation of direct electron detectors (Li et al., 2013a,b; Campbell et al., 2012; Bai et al., 2013) enables acquisition of exposure series and allows higher resolution reconstructions with fewer particles for SPA. Such acquisition facilitates reduction of the effect of beam induced movements by retrospective alignment and then averaging of the raw frames. This correction could be applied to tilt-series data collection as well. Nevertheless, each projection in a tilt series is acquired with a significantly smaller electron dose than in SPA. The extremely low SNR will severely hamper alignment of the sub-frames within a projection in a tilt-series. In order to process such data one would need a modified data acquisition, an independent set of gold markers dedicated to frame alignment and/or a mathematical model able to predict the radiation damage.

Using our simulations we give an estimate of the influence of a direct electron detector in counting mode (*perfect* detector) on the final resolution. The simulated *perfect* detector when compared to a Falcon I suggests that the same resolution would be achieved with approximately half the number of particles (dotted line in Fig. 4).

We conclude from our simulations that the following set of requirements should be fulfilled in order to achieve a resolution of approximately 1 nm using subtomogram averaged CET: (i) 40,000 asymmetrical subunits (possibly 20,000 when using the latest generation of direct electron detectors), (ii) CTF correction which accounts for the defocus gradient induced by tilting, (iii) defocus estimation accuracy of $\leq$100 nm, (iv) tilt-series alignment better than 0.2 nm and (v) estimation of subtomogram orientation with an accuracy of $\leq 1^\circ$ (depending on size of particle).

Author contributions

B.R., L.J.vV., E.M.F. and P.J.P. supervised research, M.M. acquired experimental data, M.M. and L.M.V. reconstructed experimental data, A.S. prepared ribosome samples, A.V. implemented extended acquisition scheme, M.V. performed tilt-series simulations, L.M.V. theoretically predicted limits of CTF correction and defocus estimation and reconstructed simulated data, L.M.V. and M.V. performed research and analyzed data, M.M and A.S. wrote experimental methods, and L.M.V. and M.V. wrote the manuscript.

Acknowledgments

We acknowledge support from the FOM Industrial Partnership program No. 07.0599 and European Communitys Seventh Framework Program (FP7 2007–2013) under Grant agreement No. 267038. A part of this work was carried out on the Dutch national e-infrastructure with the support of SURF Foundation.

Appendix A. Supplementary data

Supplementary data associated with this article can be found, in the online version, at http://dx.doi.org/10.1016/j.jsb.2014.06.007.

References

Bai, X.C., Fernandez, I.S., McMullan, G., Scheres, S.H., 2013. Ribosome structures to near-atomic resolution from thirty thousand cryo-em particles. Elife 2.

Bartesaghi, A., Lecumberry, F., Sapiro, G., Subramaniam, S., 2012. Protein secondary structure determination by constrained single-particle cryo-electron tomography. Structure 20, 2003–2013. http://dx.doi.org/10.1016/j.str.2012.10.016.

Briggs, J.A.G., Riches, J.D., Glass, B., Bartonova, V., Zanetti, G., Kräusslich, H.G., 2009. Structure and assembly of immature HIV. Proc. Natl. Acad. Sci. 106, 11090–11095.

Brilot, A.F., Chen, J.Z., Cheng, A., Pan, J., Harrison, S.C., Potter, C.S., Carragher, B., Henderson, R., Grigorieff, N., 2012. Beam-induced motion of vitrified specimen on holey carbon film. J. Struct. Biol. 177, 630–637. http://dx.doi.org/10.1016/j.jsb.2012.02.003.

Campbell, M.G., Cheng, A., Brilot, A.F., Moeller, A., Lyumkis, D., Veesler, D., Pan, J., Harrison, S.C., Potter, C.S., Carragher, B., et al., 2012. Movies of ice-embedded particles enhance resolution in electron cryo-microscopy. Structure 20, 1823–1828.

Chen, Y., Pfeffer, S., Hrabe, T., Schuller, J.M., Förster, F., 2013. Fast and accurate reference-free alignment of subtomograms. J. Struct. Biol. 182, 235–245. http://dx.doi.org/10.1016/j.jsb.2013.03.002.

Dümmler, A., Lawrence, A.M., De Marco, A., 2005. Simplified screening for the detection of soluble fusion constructs expressed in *E. coli* using a modular set of vectors. Microb. Cell Factories 4, 34.

Eibauer, M., Hoffmann, C., Plitzko, J.M., Baumeister, W., Nickell, S., Engelhardt, H., 2012. Unraveling the structure of membrane proteins in situ by transfer function corrected cryo-electron tomography. J. Struct. Biol. 180, 488–496.

Elmlund, H., Elmlund, D., Bengio, S., 2013. PRIME: Probabilistic initial 3D model generation for single-particle cryo-electron microscopy. Structure 21, 1299–1306. http://dx.doi.org/10.1016/j.str.2013.07.002.

Fechter, P., Chevalier, C., Yusupova, G., Yusupov, M., Romby, P., Marzi, S., 2009. Ribosomal initiation complexes probed by toeprinting and effect of trans-acting translational regulators in bacteria. In: Serganov, A. (Ed.), Riboswitches, Methods in Molecular Biology, vol. 540. Humana Press, pp. 247–263.

Fernández, J.J., Li, S., Crowther, R.A., 2006. CTF determination and correction in electron cryotomography. Ultramicroscopy 106, 587–596.

Jensen, G.J., Kornberg, R.D., 2000. Defocus-gradient corrected back-projection. Ultramicroscopy 84, 57–64.

Kazantsev, I.G., Klukowska, J., Herman, G.T., Cernetic, L., 2010. Fully three-dimensional defocus-gradient corrected backprojection in cryoelectron microscopy. Ultramicroscopy 110, 1128–1142.

Kremer, J.R., Mastronarde, D.N., McIntosh, J.R., 1996. Computer visualization of three-dimensional image data using IMOD. J. Struct. Biol. 116, 71–76.

J.J. Kuffner, Effective sampling and distance metrics for 3D rigid body path planning, in: Proceedings of the IEEE International Conference on Robotics and Automation (ICRA 2004), 2009, pp. 3993–3998.

Li, X., Mooney, P., Zheng, S., Booth, C.R., Braunfeld, M.B., Gubbens, S., Agard, D.A., Cheng, Y., 2013a. Electron counting and beam-induced motion correction enable near-atomic-resolution single-particle cryo-EM. Nat. Methods 10, 584–590.

Li, X., Zheng, S.Q., Egami, K., Agard, D.A., Cheng, Y., 2013b. Influence of electron dose rate on electron counting images recorded with the K2 camera. J. Struct. Biol. 184, 251–260.

Mastronarde, D.N., 1997. Dual-axis tomography: an approach with alignment methods that preserve resolution. J. Struct. Biol. 120, 343–352. http://dx.doi.org/10.1006/jsbi.1997.3919.

McMullan, G., Chen, S., Henderson, R., Faruqi, A.R., 2009. Detective quantum efficiency of electron area detectors in electron microscopy. Ultramicroscopy 109, 1126–1143.

Nicastro, D., Schwartz, C., Pierson, J., Gaudette, R., Porter, M.E., McIntosh, J.R., 2006. The molecular architecture of axonemes revealed by cryoelectron tomography. Science.

Pettersen, E.F., Goddard, T.D., Huang, C.C., Couch, G.S., Greenblatt, D.M., Meng, E.C., Ferrin, T.E., 2004. UCSF chimera – a visualization system for exploratory research and analysis. J. Comput. Chem. 25, 1605–1612.

Philippsen, A., Engel, H.A., Engel, A., 2007. The contrast-imaging function for tilted specimens. Ultramicroscopy 107, 202–212. http://dx.doi.org/10.1016/j.ultramic.2006.07.010.

Rosenthal, P.B., Henderson, R., 2003. Optimal determination of particle orientation, absolute hand, and contrast loss in single-particle electron cryomicroscopy. J. Mol. Biol. 333, 721–745.

Scheres, S.H.W., Chen, S., 2012. Prevention of overfitting in cryo-EM structure determination. Nat. Methods 9, 853–854.

Schur, F.K.M., Hagen, W., de Marco, A., Briggs, J.A.G., 2013. Determination of protein structure at 8. 5Å resolution using cryo-electron tomography and sub-tomogram averaging.. J. Struct. Biol. 184, 394–400. http://dx.doi.org/10.1016/j.jsb.2013.10.015.

Voortman, L.M., Franken, E.M., van Vliet, L.J., Rieger, B., 2012. Fast, spatially varying CTF correction in TEM. Ultramicroscopy 118, 26–34.

Voortman, L.M., Stallinga, S., Schoenmakers, R.H.M., van Vliet, L.J., Rieger, B., 2011. A fast algorithm for computing and correcting the CTF for tilted, thick specimens in TEM. Ultramicroscopy 111, 1029–1036.

Vulović, M., Franken, E., Ravelli, R.B.G., van Vliet, L.J., Rieger, B., 2012. Precise and unbiased estimation of astigmatism and defocus in transmission electron microscopy. Ultramicroscopy 116s, 115–134. http://dx.doi.org/10.1016/j.ultramic.2012.03.004.

Vulović, M., Ravelli, R.B., van Vliet, L.J., Koster, A.J., Lazić, I., Lücken, U., Rullgård, H., Öktem, O., Rieger, B., 2013. Image formation modeling in cryo-electron microscopy. J. Struct. Biol. 183, 19–32.

Vulović, M., Rieger, B., van Vliet, L.J., Koster, A.J., Ravelli, R.B.G., 2010. A toolkit for the characterization of CCD cameras for transmission electron microscopy. Acta Crystallogr. Sect. D 66, 97–109.

Vulović, M., Voortman, L.M., van Vliet, L.J., Rieger, B., 2014. When to use the projection assumption and the weak-phase object approximation in phase contrast cryo-EM. Ultramicroscopy 136, 61–66.

Winkler, H., Taylor, K.A., 2003. Focus gradient correction applied to tilt series image data used in electron tomography. J. Struct. Biol. 143, 24–32.

Xiong, Q., Morphew, M.K., Schwartz, C.L., Hoenger, A.H., Mastronarde, D.N., 2009. CTF determination and correction for low dose tomographic tilt series. J. Struct. Biol. 168, 378–387.

Zanetti, G., Riches, J.D., Fuller, S.D., Briggs, J.A.G., 2009. Contrast transfer function correction applied to cryo-electron tomography and sub-tomogram averaging. J. Struct. Biol. 168, 305–312.

Zhang, L., Ren, G., 2012. IPET and FETR: Experimental approach for studying molecular structure dynamics by cryo-electron tomography of a single-molecule structure. PLoS ONE 7, e30249. http://dx.doi.org/10.1371/journal.pone.0030249.